High-energy proton emission and Fermi motion in intermediate-energy heavy-ion collisions

W. Lin (林炜平),[1] X. Liu (刘星泉),[1,*] R. Wada,[1,2,†] M. Huang (黄美容),[1,2] P. Ren (任培培),[1,3] G. Tian (田国玉),[1,3] F. Luo (罗飞),[1,4] Q. Sun (孙琪),[1,3] Z. Chen (陈志强),[1] G. Q. Xiao (肖国青),[1] R. Han (韩瑞),[1] F. Shi (石福栋),[1] J. Liu (刘建立),[1] and B. Gou (勾伯兴)[1]

[1]*Institute of Modern Physics, Chinese Academy of Sciences, Lanzhou 730000, China*

[2]*Cyclotron Institute, Texas A&M University, College Station, Texas 77843, USA*

[3]*University of Chinese Academy of Sciences, Beijing 100049, China*

[4]*University of Science and Technology of China, Hefei 230026, China*

(Received 12 October 2016; published 13 December 2016)

An antisymmetrized molecular dynamics model (AMD-FM), modified to take into account the Fermi motion explicitly in its nucleon-nucleon collision process, is presented. Calculated high-energy proton spectra are compared with those of ^{40}Ar + ^{51}V at 44 MeV/nucleon from Coniglione *et al.* [Phys. Lett. B **471**, 339 (2000)] and those of ^{36}Ar + ^{181}Ta at 94 MeV/nucleon from Germain *et al.* [Nucl. Phys. A **620**, 81 (1997)]. Both of the experimental data are reasonably well reproduced by the newly added Fermi boost in the nucleon-nucleon collision process without additional processes, such as a three-body collision or a short-range correlation. The production mechanism of high-energy protons in intermediate-energy heavy-ion collisions is discussed.

DOI: 10.1103/PhysRevC.94.064609

I. INTRODUCTION

In quantum mechanics, fermions obey the Pauli exclusion principle. For protons and neutrons in a nucleus, therefore, their wave packets have to be antisymmetrized. This leads nucleons in a ground-state nucleus to have a finite momentum known as the Fermi motion. In experiments, it has been reported that the momentum distribution of protons in a nucleus has a momentum distribution, which can be approximated by a Gaussian distribution with $\sigma \sim 75$–80 MeV/c [1–3]. However, it is not straight forward to take into account the Fermi motion properly in theoretical reaction simulations at intermediate-energy heavy-ion collisions, because the initial ground-state nuclei have to be stable enough, but the fluctuation for the Fermi motion can be much larger than the binding energy in the initial nuclei. Different transport models have been developed to study intermediate-energy heavy-ion collisions, such as fermionic molecular dynamics [4], antisymmetrized molecular dynamics (AMD) [5–8], constrained molecular dynamics (CoMD) [9,10], improved quantum molecular dynamics [11], stochastic mean field (SMF) [12], quantum molecular dynamics (QMD) [13], the Vlasov-Uehling-Uhlenbeck (VUU) model [14], the Boltzmann-Uehling-Uhlenbeck (BUU) model [15], and the Boltzmann-Nordelheim-Vlasov (BNV) model [16,17], among others. All of them take into account the Fermi motion in an approximated manner in the initial ground-state nuclei. In the BUU, VUU, BNV, and SMF models, a test particle method is used. In the method, a nucleon consists of typically 30–100 classical test particles. In other models, a nucleon is described by a Gaussian wave packet in coordinate and momentum space. In most models except AMD, the Fermi motion is given according to a local Fermi gas approximation under the uncertainty principle. Therefore nucleons inside the initial nuclei are actually moving relative to each other. However, because each nucleon inside the initial nuclei inherits the same Fermi motion throughout the calculation, a nucleon cannot have a large momentum to make the initial nuclei stable enough for the calculation. Therefore the distribution of the Fermi motion is limited by a sharp cutoff value or limited in a smaller value. In AMD, as discussed below, the Fermi motion is treated in a different manner.

In experiments, Coniglione *et al.* reported the energetic proton emissions in ^{40}Ar + ^{51}V at 44 MeV/nucleon using the MEDEA detector array [18] and compared the energy spectra to those of BNV calculations [19]. In their BNV model, Fermi distribution with a sharp cutoff is incorporated as the Fermi motion of the nucleons, neglecting the stability of the initial nuclei and suggesting that the Fermi motion is a possible origin for the observed high-energy protons. A similar experimental analysis was made by the same group in Ref. [20], using ^{58}Ni + ^{58}Ni at 30 MeV/nucleon at the Laboratori Nazionali del Sud in Ctania, Italy, with the MEDEA and the MULTICS [21] apparatus. In the analysis, the proton energy spectrum for the central collisions is well reproduced by the BNV calculations using a Gale-Bertsh-Das Gupta momentum-dependent interaction. However the experimentally observed quadratic increase of the energetic proton multiplicity as a function of the number of participant nucleons cannot be explained by the calculations, suggesting that there are other mechanisms besides the one-body mean-field dissipation and the two-body nucleon-nucleon (NN) collisions. Germain *et al.* reported high-energy proton emissions in ^{36}Ar + ^{181}Ta collisions at 94 MeV/nucleon [22]. In the analysis, a BNV code is used to calculate the density of nucleons during the time evolution and collisions are made in a perturbed way, using the calculated nucleon density. Because they were not able to reproduce the high-energy proton spectra by the two-body collisions alone, they added a three-body collision process in their calculation and concluded that the three-body collision term plays a significant role in reproducing the observed high-energy proton spectra.

*liuxingquan@impcas.ac.cn

†wada@comp.tamu.edu

In this article, we report the results of AMD simulations for the energetic proton productions at 44 and 94 MeV/nucleon, using AMD-FM, a modified version of AMD, in which the Fermi motion is taken into account explicitly in the dynamical time evolution through the nucleon-nucleon collision process in addition to the wave packet diffusion process built in by Ono and Horiuchi [6]. AMD-FM is briefly described in Sec. II. Detail comparisons of high-energy proton spectra and angular distributions with ^{40}Ar + ^{51}V at 44 MeV/nucleon and ^{36}Ar + ^{181}Ta at 94 MeV/nucleon are carried out in Sec. III. High-energy proton production mechanisms are discussed in Sec. IV. A summary is given in Sec. V.

II. FERMI BOOST IN AMD

A. AMD

In AMD, the Fermi motion is taken into account in quantum fluctuations [5,23]. The reaction system with N nucleons is described as a Slater determinant of N Gaussian wave packets,

$$\Phi(Z) = \det\left\{\exp\left[-\nu\left(\boldsymbol{r}_j - \frac{\boldsymbol{Z}_i}{\sqrt{\nu}}\right)^2 + \frac{1}{2}\boldsymbol{Z}_i^2\right]\chi_{\alpha_i}(j)\right\}, \quad (1)$$

where the complex variables $Z \equiv \{\boldsymbol{Z}_i;\, i = 1,\ldots,N\} = \{Z_{i\sigma};\, i = 1,\ldots,N;\, \sigma = x,y,z\}$ represent the centroids of the wave packets. χ_{α_i} represents the spin and isospin states of $p\uparrow$, $p\downarrow$, $n\uparrow$, or $n\downarrow$. The width parameter ν is taken as $\nu = 0.16$ fm^{-2} to reproduce the binding energy of nuclei properly. The experimental binding energies are reproduced within 10% for most nuclei [24]. Using the centroid of the Gaussian wave packets, the time evolution of Z is determined classically by the time-dependent variational principle and the two-body nucleon collision process. The equation of motion is described as

$$i\hbar\sum_{j\tau} C_{i\sigma,j\tau}\frac{dZ_{j\tau}}{dt} = \frac{\partial\mathcal{H}}{\partial Z^*_{i\sigma}}, \quad (2)$$

Here $\mathcal{H}$ is the Hamiltonian. $C_{i\sigma,j\tau}$ is a Hermitian matrix defined by

$$C_{i\sigma,j\tau} = \frac{\partial^2}{\partial Z^*_{i\sigma}\partial Z_{j\tau}}\log\langle\Phi(\mathbf{Z})|\Phi(\mathbf{Z})\rangle. \quad (3)$$

In AMD, the centroid of the wave packet in the momentum space in the initial nuclei is set to nearly 0. This means that the initial nuclei are "frozen" and makes the initial nuclei stable in time. The Fermi motion is taken into account in the time evolution through the wave-packet diffusion (and shrinking) processes [6,8]. As described in detail in the references, this process is taken into account stochastically in the time evolution of the wave packets to make a proper multifragmentation of hot nuclear matter generated during collisions.

AMD treats a nucleon-nucleon collision process in the physical space. The physical coordinates $W \equiv \{\boldsymbol{W}_i\}$ are calculated approximately as $\boldsymbol{W}_i = \sum_{i=1}^{N}(\sqrt{Q})_{ij}\boldsymbol{Z}_j$. Here

$$Q_{ij} = \frac{\partial}{\partial(Z^*_i Z_j)}\ln\langle\Phi(\mathbf{Z})|\Phi(\mathbf{Z})\rangle. \quad (4)$$

W coordinates have a one-to-one correspondence to physical N nucleons. In a Wigner form, the ith nucleon at time $t = t_0$ is represented as

$$f_i(\boldsymbol{r},\boldsymbol{p},t_0) = 8\exp\left\{-2\nu[\boldsymbol{r} - \boldsymbol{R}_i(t_0)]^2 - \frac{[\boldsymbol{p} - \boldsymbol{P}_i(t_0)]^2}{2\hbar^2\nu}\right\}, \quad (5)$$

with the centroid $\boldsymbol{R}_i$ and $\boldsymbol{P}_i$. The total one-body distribution function is the sum of f_i. This representation is valid only approximately when the physical coordinate

$$\boldsymbol{W}_i = \sqrt{\nu}\boldsymbol{R}_i + \frac{i}{2\hbar\sqrt{\nu}}\boldsymbol{P}_i \quad (6)$$

is used for the centroid of the Gaussian wave packets [5].

In AMD calculations, similar to other transport models, there are two separate processes, one is the mean-field propagation of nucleons and the other is the NN collision process. The mean-field propagation is governed by a given effective interaction and the NN collision rate is determined by a given NN cross section. In AMD, the Pauli principle is fully respected in an exact manner in both processes. Throughout this article, the Gogny interaction [5] is used for the mean field. The nucleon-nucleon cross section is given by [8]

$$\sigma(E,\rho) = \min\left(\sigma_{\rm LM}(E,\rho),\, \frac{100\text{ mb}}{1 + E/(200\text{ MeV})}\right), \quad (7)$$

where $\sigma_{\rm LM}(E,\rho)$ is the cross section given by Li and Machleidt [25]. The angular distributions of proton-neutron scattering are parametrized as

$$\frac{d\sigma_{pn}}{d\Omega} \propto 10^{-\alpha(\pi/2-|\theta-\pi/2|)},$$
$$\alpha = \frac{2}{\pi}\max\{0.333\ln E[\text{MeV}] - 1,\, 0\}, \quad (8)$$

while the proton-proton and neutron-neutron scatterings are assumed to be isotropic.

The AMD model has been extended by introducing the wave-packet diffusion [6] and shrinking [7] processes as a quantum branching process of the wave packets to treat properly the multifragmentation process. In the present simulations, the version in Ref. [6] is used, in which the only diffusion process is taken into account. The time-dependent many-body wave function, described by Eq. (1) for a complicated nuclear collision, is a superposition of a huge number of channels, each of which corresponds to a different clusterization configuration. The time evolution in AMD described in Refs. [6,7] is determined by two factors, the mean-field propagation and the decomposition into branches (quantum branching). The latter is treated numerically as follows. By simply introducing the parameter c and the normalized function g(ξ), which depend on $\Phi[Z(t_0)]$, δt, and i, the diffusion of wave packets in one-body distribution function at $t = t_0 + \delta t$ can be written as a superposition of Gaussian functions as

$$f_i(x,t_0+\delta t) = (1-c)F[x - X_i(t_0+\delta t)] + \int \text{g}(\xi)F[x - X_i(t_0+\delta t) - \xi]d\xi, \quad (9)$$

where

$$F(x) = \prod_{a=1}^{6} \sqrt{2/\pi} e^{-2x_a^2}, \tag{10}$$

$$x = \{x_a\}_{a=1,\ldots,6} = \left\{ \sqrt{\nu}\mathbf{r}, \frac{\mathbf{p}}{2\hbar\sqrt{\nu}} \right\}, \tag{11}$$

$$X_i = \{X_{ia}\}_{a=1,\ldots,6} = \left\{ \sqrt{\nu}\mathbf{R}_i, \frac{\mathbf{P}_i}{2\hbar\sqrt{\nu}} \right\}. \tag{12}$$

By restricting $g(\xi) \geqslant 0$ and $0 \leqslant c \leqslant 1$, the diffusion of the wave packets is described consistently. For more details about the quantum branching, we refer to Refs. [6,7]. The physical origin of the quantum branching is to take into account the quantum fluctuation in phase space as seen in the above formulation. The branching of wave packets to decomposed states originates from this fluctuation in the time evolution of the wave packets. Fermi boost taken into account in the two-body collision process as described in the next section originates from the same nucleon-nucleon interaction, but in AMD in Ref. [6] the diffusion process and the two-body collision process are treated as independent processes. Therefore we need to take into account the quantum fluctuation as the Fermi boost in both processes.

As suggested by Coniglione *et al.* [19], the high-energy protons may be generated by incoherent nucleon-nucleon collisions at a very early stage of the collisions. Therefore it is important to take into account the momentum distribution (Fermi motion) explicitly as the Fermi boost in the collision process.

B. Fermi boost in AMD-FM

In AMD, the wave-packet propagation in time is performed classically, solving the Vlasov equation for the centroids of the wave packets with a stochastic two-body collision process. To take into account the momentum distribution of the wave packets explicitly in the collision process, the Gaussian distribution of the momentum is interpreted quantum mechanically as the probability distribution of the momentum for each nucleon. When two nucleons are at the collision distance $\sqrt{(\sigma_{NN})/\pi}$, the momentum uncertainty increases. This uncertainty of the momentum is given along the Gaussian distribution around the centroid. This process is repeated for every collision. This treatment is quite different from those in other transport models, in which the Fermi motion is given only once in the initial nuclei. Our treatment is based on the experimental observation of $(e,e'p)$ reactions [2,3]. In the $(e,e'p)$ experiments, electrons were bombarded on a target nuclei, the scattered electron and emitted proton were measured in coincidence mode, and the missing momentum was reduced in the reaction. The observed experimental spectra have been modeled by a quasifree knockout picture, using mean-field calculations such as the distorted-wave impulse approximation, and the spectra were well reproduced below 250 MeV/c. In a direct knockout picture, this missing momentum is closely related to the momentum distribution of the protons in the ground state of the target nucleus, which we call "Fermi motion" in this article. Along the transport model picture, we fitted the high-energy tail of the experimental spectra by a Maxwell-Boltzmann distribution with a σ of $\sim$75 MeV/c for $P_p \leqslant 400$ MeV/c as seen in Fig. 1.

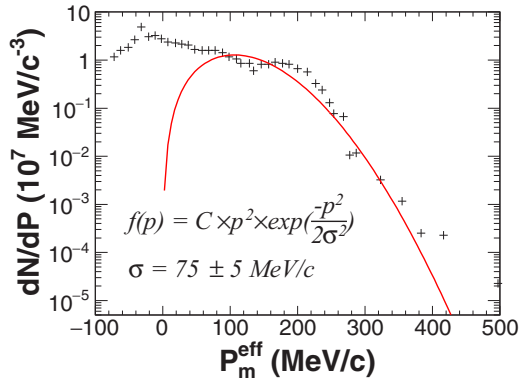

FIG. 1. The Fermi momentum distribution from the $(e,e'p)$ experiment with a Maxwell-Boltzmann fit. The experimental data are taken from Bobeldijk *et al.* [2,3].

We interpret this observation that a nucleon in a ground-state nucleus have a momentum distribution of Gaussian distribution as a probability distribution. When the momentum is probed from outside by an electron, photon, or nucleon, for example, proton momentum appears as $\boldsymbol{P}_0 + \Delta\boldsymbol{P}$, where $\boldsymbol{P}_0$ is the centroid of the Gaussian distribution and $\Delta\boldsymbol{P}$ is a fluctuation given by the Gaussian distribution. It is interesting to note that, in AMD, the width of the momentum distribution is determined from the uncertainty relation $\sigma_r\sigma_p = \hbar/2$ and $\sigma_r = 1/2\sqrt{\nu}$. This results in $\sigma_p = \hbar\sqrt{\nu}$. As mentioned earlier, ν is optimized as a free parameter to reproduce the experimental binding energy of nuclei and $\nu = 0.16$ fm^{-2} is taken for the Gogny interaction. This ends up as $\sigma_p = 78.9$ MeV/c, which is consistent with the value obtained from the $(e,e'p)$ experiment described above. Therefore in this article the momentum uncertainty given by the Gaussian distribution with σ_p is called "Fermi motion," and the effect caused by this momentum fluctuation is called "Fermi boost."

In the actual calculation for given coordinate vectors $\boldsymbol{r}_1$ and $\boldsymbol{r}_2$ of two attempted colliding nucleons, the associated momenta $\boldsymbol{P}_1$ and $\boldsymbol{P}_2$ are given as

$$\boldsymbol{P}_i = \boldsymbol{P}_i^0 + \Delta\boldsymbol{P}_i' \quad (i = 1,2). \tag{13}$$

$\boldsymbol{P}_i^0$ is the centroid of the Gaussian momentum distribution for the particle i. The second term $\Delta\boldsymbol{P}_i'$ is the Fermi momentum randomly given along the Gaussian distribution. Because the momentum distribution is partially taken into account in the wave-packet propagation through the diffusion process, we subtract T_0 from $\Delta\boldsymbol{P}_i'$ to avoid a double counting. The $T_0 = 3\hbar^2\nu/2M_0 \sim 10$ MeV originally corresponds to the expectation value of the mean energy for the Gaussian distribution, but is slightly adjusted for a given effective interaction to optimize the binding energy. For the Gogny interaction, $T_0 = 9.20$ MeV is taken. After subtracting T_0, $\Delta\boldsymbol{P}_i'$

is calculated as

$$\Delta \boldsymbol{P}_i' = \sqrt{\left(\frac{|\Delta \boldsymbol{P}_i|^2}{2M_0} - T_0\right)2M_0}\frac{\Delta \boldsymbol{P}_i}{|\Delta \boldsymbol{P}_i|},$$
$$\Delta P_{i\tau} = \hbar\sqrt{\nu}(\rho_i/\rho_0)^{1/3}G(1), \quad (14)$$

where $G(1)$ is a random number generated along the Gaussian distribution with $\sigma = 1$. $(\rho_i/\rho_0)^{1/3}$ in Eq. (14) is used for taking into account the density dependence of the Fermi energy. ρ_i is the density at $\boldsymbol{r}_i$ and ρ_0 is the normal nuclear density. The index τ corresponds to the x, y, and z coordinates. When $|\Delta \boldsymbol{P}_i'|^2/2M_0 < T_0$, $\Delta \boldsymbol{P}_i'$ sets to 0.

When the collision is Pauli blocked, the treatment in the W space is canceled and the time evolution of wave packets continues in the Z space. When the collision is Pauli allowed, the momentum and energy conservations are restored. The momentum restoration is made assuming a long-range correlation mechanism between nucleons in the cluster in which the two colliding nucleons belong. To do that, the system is clusterized at the time using a coalescence technique in coordinate space with a radius of 5 fm. One should note that this clusterization is irrelevant to the time evolution of the wave packets in the AMD calculation; that is, this process is only performed to acquire the cluster information at the time when the collision is tested.

The energy restoration is also performed within the cluster. The energy correction is made by

$$\Delta E = \left(\sum_{i,\sigma}\frac{\partial \mathcal{H}}{\partial Z_{i,\sigma}}\frac{dZ_{i,\sigma}}{dt}\right)\Delta t,$$

using Δt as an artificial fine step for turning. The $\mathcal{H}$ is the Hamiltonian of the cluster. The summation is taken over all nucleons in the cluster. To show the precision of the correction, the total energy of the system is shown as a function of time for AMD and AMD-FM in Fig. 2. As one can see, the energy restoration after the collisions is very good up to $t = 200$ fm/c. The restoration starts to fail for some events after that, though the failure is still on an order of a few tens of MeV. Therefore in the following sections, the proton energy is evaluated at $t = 200$ fm/c.

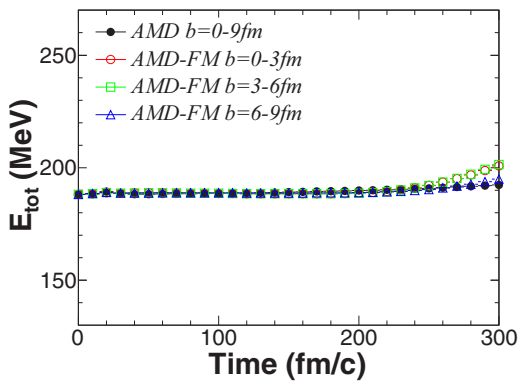

FIG. 2. The total energy of the system as a function of time for AMD with $b = 0$–9 fm (closed circles) and AMD-FM with $b = 0$–3 fm (open circles), $b = 3$–6 fm (open squares), and $b = 6$–9 fm (open triangles).

III. RESULTS

Before we presents the results of the new AMD-FM calculations, we first compare the experimental results of ^{40}Ar+^{51}V at 44 MeV/nucleon [19] to those of ordinary AMD and CoMD simulations. In CoMD, a process is added to QMD to prevent the violation of the Pauli principle in the wave-packet propagation in time in a stochastic manner [9,10]. Different from AMD, in CoMD the Fermi motion is explicitly taken in the initial ground-state nuclei. When the initial nuclei are prepared, the momentum is assigned to each nucleon under a local Fermi gas assumption. To get enough stability during calculations with a proper binding energy of these nuclei, the nuclei are further cooled by a friction method [5,26,27]. Therefore the momentum distribution values become much smaller in the initial nuclei. In Fig. 3, the experimental results are compared with those of (a) AMD and (b) CoMD simulations with the impact parameter range of 0–9 fm. The comparisons are made in an absolute scale. In Fig. 3 it is clearly shown that neither AMD nor CoMD calculations can reproduce the experimental high-energy proton spectra in their slopes and amplitudes. One should note that, in the AMD results, the calculated spectra have slightly harder slopes than those of CoMD, even though the initial nuclei are "frozen" in the AMD calculation. This enhancement is caused from the diffusion process discussed earlier.

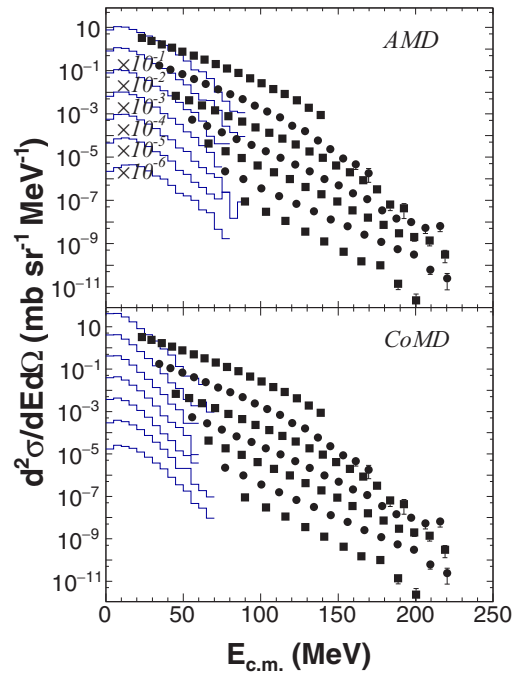

FIG. 3. The center-of-mass frame proton energy spectra of AMD (a) and CoMD (b) in an absolute scale are compared with the experimentally observed inclusive data (solid symbols) of ^{40}Ar+^{51}V at 44 MeV/nucleon at $\theta = 72^\circ, 90^\circ, 104^\circ, 116^\circ, 128^\circ, 142^\circ$, and 160° from top to bottom. The experimental data are taken from Coniglione *et al.* [19].

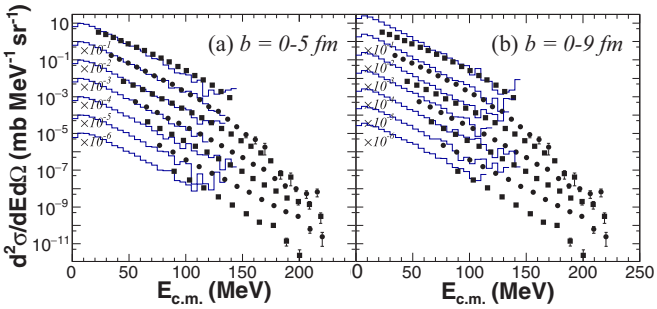

FIG. 4. Proton energy spectra of the AMD-FM calculation for (a) $b = 0$–5 fm and (b) $b = 0$–9 fm are compared in an absolute scale with the experimentally observed inclusive data (solid symbols) of ^{40}Ar + ^{51}V at 44 MeV/nucleon at different angles in the center-of-mass frame. The angles are $\theta = 72^\circ$, 90°, 104°,116°, 128°, 142°, and 160° from top to bottom. The experimental data are taken from Congilione *et al.* [19].

Figure 4 shows the comparisons between the experimental proton energy spectra and those of AMD-FM with $b = 0$–5 fm in panel (a) and $b = 0$–9 fm in panel (b) in an absolute scale. The experimental data are inclusive. A few hundred thousand events have been generated for the AMD-FM calculation. No afterburner is used in the analysis presented here, because high-energy protons are essentially generated in the Fermi boost in the nucleon propagation in the mean field through the defusion process and that in the NN collision process as discussed in Sec. IV. The results for $b = 0$–5 fm are in good agreement with the experimental data. If the impact parameter range of $b = 0$–9 fm is used, the calculated cross sections become about twice larger at four forward angles. In either case of the impact parameter range, the high-energy proton generation in its amplitude and energy slope is significantly improved by adding the Fermi boost in the NN collision process. This indicates that at 44 MeV/nucleon, the high-energy protons are well reproduced by adding the Fermi boost in the collision process, which is characterized by the Gaussian distribution with a σ of $\sim$78.9 MeV/c.

The available experimental angular distribution and energy spectra in the center-of-mass system are also compared with those of the AMD-FM calculation for central collisions. The angular distribution, which has been normalized to their mean value, of energetic protons ($90 \leqslant E_p^{NN} \leqslant 110$ MeV) from AMD-FM (open squares) and that of the experiment (solid squares) are compared in Fig. 5. The impact parameter range of $b = 0$–3 fm used for AMD-FM is comparable to that of $b/b_{\max} = 0$–0.18 for the experiment. The AMD-FM results show slightly flatter distribution, though the statistical error bars are large. In Fig. 6. the proton energy spectrum of AMD-FM at $\theta = 110^\circ \pm 10^\circ$ (open squares) is compared to the experimental spectrum (solid squares) in the center-of-mass frame for the central collision events. Because the system is nearly symmetric, to increase the statistics in the calculation, the energy spectrum integrated over 4π solid angle (open circles) are also shown in the figure. These comparisons are made in an absolute scale. The experimental energy slope is well reproduced both for the spectrum at $\theta = 110^\circ \pm 10^\circ$

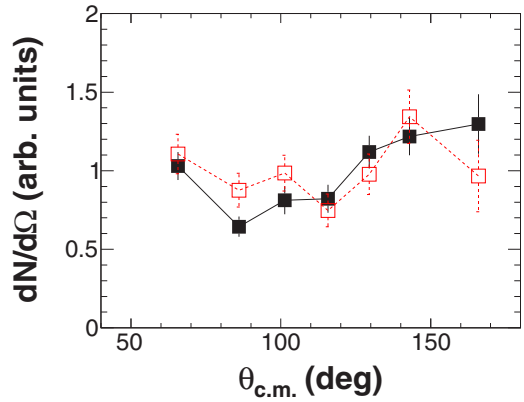

FIG. 5. Angular distribution of the cross section of energetic protons ($90 \leqslant E_p^{NN} \leqslant 110$ MeV), which have been normalized to their mean value, from AMD-FM (open triangles) are compared to the experimental data (solid squares) for ^{40}Ar + ^{51}V at 44 MeV/nucleon in the center-of-mass frame. The experimental data are taken from Coniglione *et al.* [19].

and that integrated over the 4π solid angle, but the absolute multiplicity is slightly underestimated in most of the energy range by a factor of 1.5–2 for both cases.

It is interesting to extend the comparisons at higher incident energies. As discussed in the next section, the high-energy protons are generated at an early stage of the collisions where the nuclear density is high for central collisions. If the three-body collisions contribute, the contribution becomes more significant at higher incident energy, because the three-body collisions occur in proportion to the third power of the nuclear density whereas the two-body collisions to the second power [16]. However one should be cautious to introduce a new mechanism. One has to examine carefully whether the existing mechanism cannot reproduce the experimental data at all, just like we did in Figs. 3 and 4 for AMD and AMD-FM. To test the validity of AMD-FM at higher incident energies, the experimental data of ^{36}Ar + ^{181}Ta at 94 MeV/nucleon

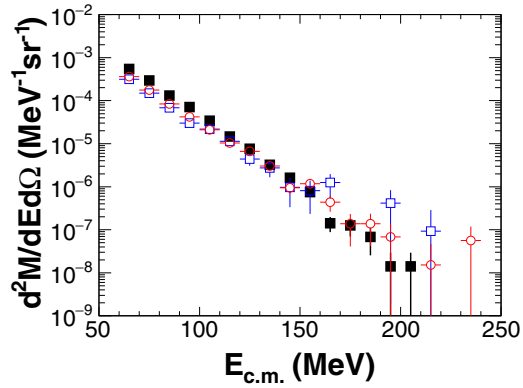

FIG. 6. Proton energy spectra of AMD-FM at $\theta \sim 110^\circ$ (open squares) and 4π solid angle (open circles) are compared to the experimental spectrum (solid squares) in the center-of-mass frame for the central collision events. The experimental data are taken from Coniglione *et al.* [19].

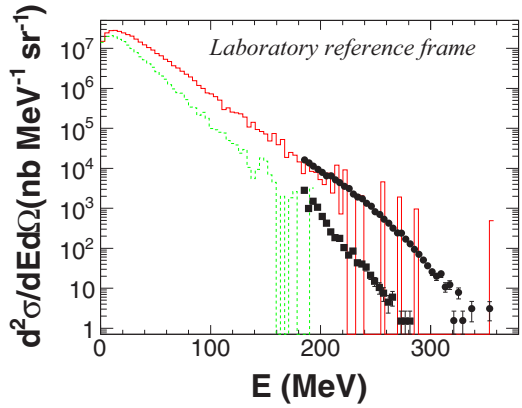

FIG. 7. Proton energy spectra of AMD-FM at 75° (red solid histogram) and 105° (green dashed histogram) are compared to those of experiment (solid symbols) in the laboratory frame for ^{36}Ar + ^{181}Ta at 94 MeV/nucleon. The experimental data are taken from Germain *et al.* [22].

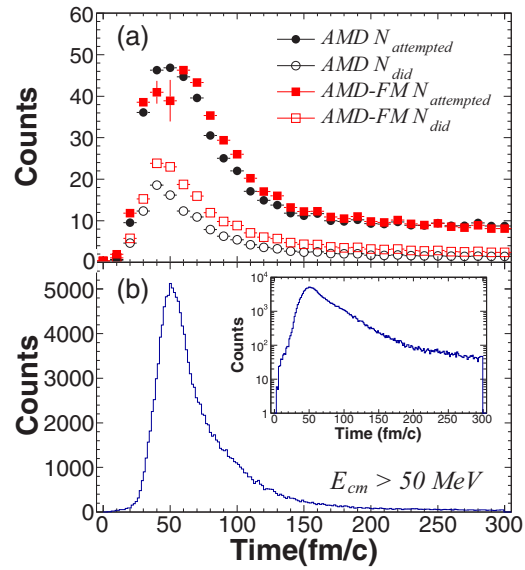

FIG. 8. (a) The number of attempted and successful collisions as a function of time. Counts are for every 10 fm/c time interval. (b) The collision time distribution of two collision nucleons in which at least one of them has energy greater than 50 MeV in the center-of-mass frame after collision for ^{40}Ar + ^{51}V at 44 MeV/nucleon. The inset histogram is the same as that in panel (b) but in logarithmic scale.

by Germain *et al.* [22] are used. The experimental data are inclusive, and therefore the impact parameter range of $b = 0$–9 fm is used for the AMD-FM calculation. About 100 000 events are generated. The calculation is ∼10 times more CPU time-consuming, compared to the time needed for the same amount of events for ^{40}Ar + ^{51}V at 44 MeV/nucleon. The calculated proton energy spectra with AMD-FM at 75° (red histogram) and 105° (green histogram) are plotted in Fig. 7 in the laboratory reference frame together with those of the experiment (solid symbols) in an absolute scale. The spectra for the AMD-FM calculation are obtained over the angular interval of ±10° at each angle. Though the statistic is still not enough for detailed comparisons, one can see that the slope and amplitude of the experimental energy spectra are reproduced reasonably by AMD-FM at 75°. If the smooth extrapolation of the slope is allowed for the calculated spectrum at 105°, the experimental data are also reasonably well reproduced. To make more accurate comparisons, another 10–100 times statistics is needed for the AMD-FM calculation but this is beyond our present CPU capability. However as seen in Fig. 6, the slope of the high-energy proton spectra is essentially determined by the Gaussian distribution of momentum used for the Fermi boost, and the smooth connection of the calculated energy slope to the experimental data supports the conclusion that the high-energy protons observed at 94 MeV/nucleon originates essentially from the Fermi boost. However, from this comparison, we cannot exclude the necessity of the three-body collision term, but the contribution is small even if it contributes some.

IV. PRODUCTION MECHANISM OF HIGH-ENERGY PROTONS AND DISCUSSIONS

In this section we further investigate the production mechanism of the high-energy proton at 44 MeV/nucleon, using the AMD-FM calculation. In Fig. 8(a), the number of attempted and Pauli-allowed collisions are plotted as a function of time. About 50–60% of attempted collisions are blocked near the peak at ∼50 fm/c and about 80% are blocked after 100 fm/c where the time zero is set about 20 fm/c before the projectile and target are in the touching radius. The average number of Pauli-allowed collisions is about 1.5 collisions per nucleon in AMD and about 2.5 in AMD-FM in the time range of 0 < time < 200 fm/c. The number of Pauli-allowed collisions from the AMD-FM calculation slightly increases compared to that from the AMD calculation. In Fig. 8(b), the time distribution is plotted when one of the nucleons has energy greater than 50 MeV in the center-of-mass frame after a collision. The distribution shows a much sharper peak around 50 fm/c and more than 80% of these collisions occur before 100 fm/c. This indicates that the high-energy protons are indeed generated by the Fermi boost at an early stage of the reaction.

In Fig. 9, the energy spectra of nucleons with energy $E_{\rm cm}$ > 50 MeV after collisions are plotted with the experimental results (red solid squares) shown in Fig. 6. The black histogram represents the spectrum for those which have $E_{\rm cm}$ > 50 MeV at the first collision (single collision). Red, green, and blue histograms are those corresponding to the second, third, and fourth collisions, respectively. One can see from the figure that the slopes of the four spectra are very similar. This indicates that the high-energy proton spectra are almost independent of the number of collisions suffered before the nucleon has energy $E_{\rm cm}$ > 50 MeV.

To further clarify the production mechanism of high-energy protons in AMD-FM, a two-dimensional plot of $E_{\rm cm}$ versus $\Delta \boldsymbol{P}_>$ is plotted in Fig. 10 when a nucleon has energy $E_{\rm cm}$ > 50 MeV at the first collision. $\Delta \boldsymbol{P}_>$ is the larger values of $\Delta \boldsymbol{P}_i$ ($i = 1$ and 2) in Eq. (13). Note that $E_{\rm cm}$ picked in this plot is not necessarily the energy for the ejected nucleons. Many of them are in fact the energy inside the nuclear matter.

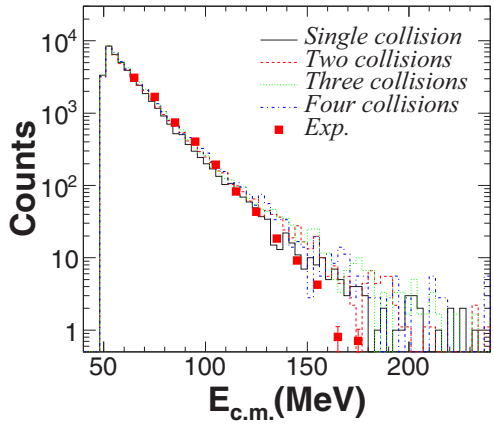

FIG. 9. The energy spectra of nucleons with $E_{\rm cm} > 50$ MeV after a collision after single (solid black histogram), two (dashed red histogram), three (dotted green histogram), and four (dot-dashed blue histogram) collisions. The spectra are normalized to the single collision at the maximum bin counts. The experimental data are taken from Coniglione *et al.* [19].

From this figure, we made two observations. There is a broad correlation of high-energy protons $E_{\rm cm}$ and high $\Delta \boldsymbol{P}_{>}$ values. The range of $\Delta \boldsymbol{P}_{>}$ is between 250 and 360 MeV/c, when $E_{\rm cm} > 150$ MeV. The other observation is that many collisions with $\Delta \boldsymbol{P}_{>} > 350$ MeV/c do not necessary end up in high-energy nucleon production. One should note that the momentum range sampled as the Fermi boost in the collision process is up to 400 MeV/c, which is much larger than that corresponding to the Fermi energy (∼270 MeV/c) normally taken as the sharp cutoff momentum value in a local Fermi gas model.

To shed further light on the high-energy proton production mechanism, some protons are picked as typical examples when the proton is ejected at $E_{\rm cm} > 100$ MeV and their energy versus time is plotted in Fig. 11. In Fig. 11(a), the kinetic energy of a proton increases ∼90 MeV after the first collision at

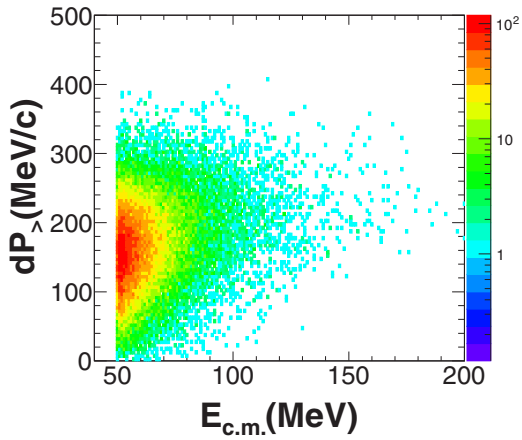

FIG. 10. The energy ($E_{\rm cm}$) versus the sampled momentum for nucleons which have $E_{\rm cm} > 50$ MeV at their first collision. There are two sampled $\Delta \boldsymbol{P}$ for two colliding nucleons. The larger one is plotted in this figure.

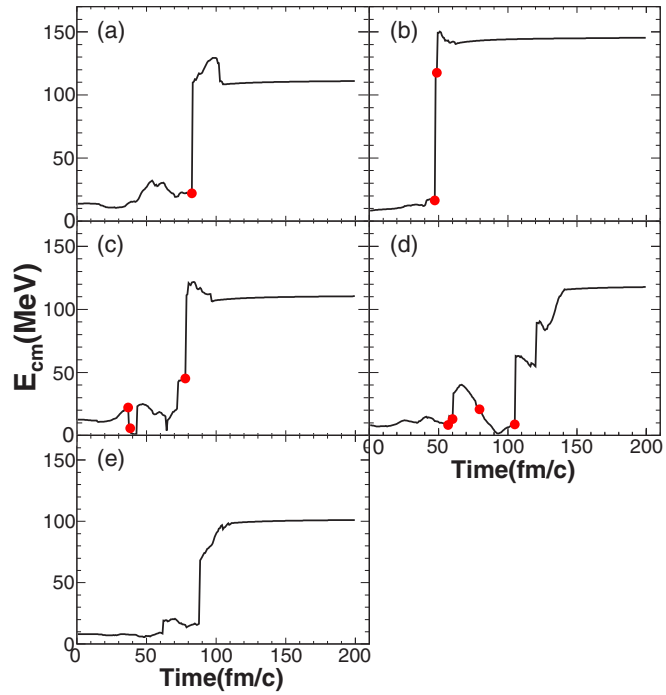

FIG. 11. The energy $E_{\rm cm}$ versus time for a nucleon ejected with $E_{\rm cm} > 100$ MeV as a function of the reaction time. Dots indicate time and energy when the collision occurred. A nucleon ejected (a) by single collision, (b) by two consecutive collisions, (c) by a collision + diffusion, (d) by a collision + two diffusions, and (e) without collisions. The solid circles represent the time at which the collisions happened.

$t \sim 80$ fm/c. The energy changes in a range of 20 MeV before the ejection in the wave-packet propagation in the effective mean field (one-body interaction) and the proton is finally ejected with $E_{\rm cm} \sim 110$ MeV at $t \sim 100$ fm/c. Once the proton is ejected, the energy becomes constant. In Fig. 11(b), a proton is ejected by two consecutive collisions at $t \sim 50$ fm/c. In Fig. 11(c) a proton is ejected by a mean-field interaction + a collision. In Fig. 11(d) a proton has $E_{\rm cm} \sim 60$ MeV after a collision followed by two consecutive jumps and rapid increases and is ejected with $E_{\rm cm} \sim 110$ MeV. In Fig. 11(e) a proton has $E_{\rm cm} \sim 100$ MeV without collisions. The energy jump or rapid increase without a collision is the result of the built-in diffusion process in AMD. The mean-field propagation without the diffusion process results in smooth energy changes in the time evolution. The diffusion process is examined in a stochastic manner and, when the quantum branching occurs, it can cause an energy jump or a rapid increase in time. However, in many cases, because the size of the fluctuation distributes along the Gaussian distribution, the energy changes through the diffusion process are small and smooth, and therefore they are not distinguishable from the mean-field propagation without the diffusion process. Here we call it the Fermi boost in the diffusion process when the proton energy changes more than 20 MeV within the time interval of 1–5 fm/c without collisions (jumps or rapid increases).

To illustrate the importance of the different ejection processes shown in the above examples, the occurrences of

TABLE I. Occurrences of different types.

Type	Occurrences
(a) Single collision	21
(b) Multiple collisions	29
(c) A collision + a diffusion	17
(d) Multiple collisions + multiple diffusions	31
(e) Without collisions	1

each type from (a)–(e) (see Table I) are counted among 930 000 protons in 22 800 events, which are only a part of the data set. In this data set, 99 protons are ejected above 100 MeV in the center-of-mass system. The occurrences for the different types are summarized in Table I. One should note that these numbers are rough estimates from the plotted figures like in Fig. 11, and sometimes it is difficult to identify the definite type.

These examples clearly show that the high-energy proton production in AMD-FM is the coplay of the Fermi boost in the diffusion process and in the collision process. However 98 events are caused by at least a single collision and only one event is observed by the diffusion process alone. Therefore the Fermi boost in the collision process is more important for the high-energy protons' generation in the intermediate-energy heavy-ion collision at $40 < E_{\rm inc} < 100$ MeV/nucleon.

In Ref. [20], Sapienza *et al.* observed a quadratic increase of the energetic proton multiplicity as a function of the number of participant nucleons, determined from the γ multiplicity. In the AMD simulations, the relation between the impact parameter and the number of the participant nucleons is not necessarily linear because of the manifestation of the semitransparency in intermediate-energy heavy-ion collisions [28,29]. Therefore we did not pursue this issue in this article. However the present analysis excludes the hypothesis that the quadratic increase originates from the three-body collisions, because no significant increase of the energetic proton yield is observed in the higher incident energies where a more significant contribution of the three-body collisions is expected.

In Ref. [22], the authors claimed that the experimental data cannot be reproduced by a binary collision process alone in their simulation, using the BNV model with a sharp cutoff Fermi distribution of the cutoff momentum of 270 MeV/c, and that the introduction of the three-body collision term is necessary to reproduce the observed slope and multiplicity. However in comparison with the actual sampled momentum distribution shown in Fig. 10, the 270 MeV/c cutoff momentum is not high enough to reproduce the experimental energy spectra. This indicates that the high-momentum tail in the Fermi distribution plays a crucial role in producing the high-energy nucleons in intermediate-energy heavy-ion collisions.

V. SUMMARY

The results of AMD-FM are presented, in which the explicit treatment of the Fermi motion is made in the collision process. The calculated results are compared with the available experimental data of ^{40}Ar + ^{51}V at 44 MeV/nucleon and ^{36}Ar + ^{181}Ta at 94 MeV/nucleon. The experimental energetic proton spectra for both systems are reasonably well reproduced. There is good agreement of the slope in all spectra between the experimental inclusive spectra and calculated ones for the ^{40}Ar + ^{51}V system. The energy slope and angular distribution are also found to be reasonably well reproduced in central collisions. These results indicate that the Fermi boost is important for the high-energy proton production in the incident energy range of 40–100 MeV/nucleon. Further detailed study indicates that the high-energy proton production is the result of coplay between the Fermi boost in the diffusion process and that in the collision process in this energy range. However our results do not exclude other production mechanisms, such as the three-body collision mechanism or short-range nucleon-nucleon correlation, especially for incident energies higher than 100 MeV/nucleon [16,17,30].

ACKNOWLEDGMENTS

We thank A. Ono for providing his AMD code and helpful discussions. We also thank A. Bonasera for useful discussion. This work is supported by the National Natural Science Foundation of China (Grants No. 91426301 and No. 11075189), the Strategic Priority Research Program of the Chinese Academy of Sciences "ADS Project" (Grant No. XDA03030200), and the Program for the CAS "Light of West China" (Grant No. Y601030XB0). This work is also supported by the U.S. Department of Energy under Grant No. DE–FG02–93ER40773. One of the authors (R.W.) thanks the program of the "Visiting Professorship of Senior International Scientists of the Chinese Academy of Sciences" for their support during his stay at IMP.

[1] D. E. Greiner *et al.*, Phys. Rev. Lett. **35**, 152 (1975).
[2] I. Bobeldijk *et al.*, Phys. Rev. Lett. **73**, 2684 (1994).
[3] I. Bobeldijk *et al.*, Phys. Lett. B **353**, 32 (1995).
[4] H. Feldmeier, Nucl. Phys. A **515**, 147 (1990).
[5] A. Ono, H. Horiuchi, T. Maruyama, and A. Ohnishi, Prog. Theor. Phys. **87**, 1185 (1992).
[6] A. Ono and H. Horiuchi, Phys. Rev. C **53**, 2958 (1996).
[7] A. Ono, Phys. Rev. C **59**, 853 (1999).
[8] A. Ono, S. Hudan, A. Chbihi, and J. D. Frankland, Phys. Rev. C **66**, 014603 (2002).
[9] M. Papa, T. Maruyama, and A. Bonasera, Phys. Rev. C **64**, 024612 (2001).
[10] M. Papa, G. Giuliani, and A. Bonasera, J. Comput. Phys. **208**, 403 (2005).
[11] N. Wang, Z. Li, and X. Wu, Phys. Rev. C **65**, 064608 (2002).
[12] M. Colonna *et al.*, Nucl. Phys. A **642**, 449 (1998).
[13] J. Aichelin, Phys. Rep. **202**, 233 (1991).
[14] H. Kruse, B. V. Jacak, J. J. Molitoris, G. D. Westfall, and H. Stöcker, Phys. Rev. C **31**, 1770 (1985).
[15] J. Aichelin and G. Bertsch, Phys. Rev. C **31**, 1730 (1985).

[16] A. Bonasera *et al.*, Phys. Lett. B **259**, 399 (1991)
[17] A. Bonasera *et al.*, Phys. Rep. **243**, 1 (1994).
[18] E. Migneco *et al.*, Nucl. Instrum. Methods Phys. Res., Sect. A **314**, 31 (1992).
[19] R. Coniglione *et al.*, Phys. Lett. B **471**, 339 (2000).
[20] P. Sapienza *et al.*, Phys. Rev. Lett. **87**, 072701 (2001).
[21] I. Iori *et al.*, Nucl. Instrum. Methods Phys. Res., Sect. A **325**, 458 (1993).
[22] M. Germain *et al.*, Nucl. Phys. A **620**, 81 (1997).
[23] A. Ono and H. Horiuchi, Prog. Part. Nucl. Phys. **53**, 501 (2004).
[24] A. Ono, P. Danielewicz, W. A. Friedman, W. G. Lynch, and M. B. Tsang, Phys. Rev. C **70**, 041604(R) (2004).
[25] G. Q. Li and R. Machleidt, Phys. Rev. C **48**, 1702 (1993); **49**, 566 (1994).
[26] L. Wilet, E. M. Henley, M. Kraft, and A. D. MacKellar, Nucl. Phys. A **282**, 341 (1977).
[27] H. Horiuchi, Nucl. Phys. A **522**, 257c (1991).
[28] R. Wada *et al.*, Phys. Rev. C **62**, 034601 (2000).
[29] R. Wada *et al.*, Phys. Rev. C **69**, 044610 (2004).
[30] E. Piasetzky, M. Sargsian, L. Frankfurt, M. Strikman, and J. W. Watson, Phys. Rev. Lett. **97**, 162504 (2006).